Water Resources Research

Supporting Information for

The Influence of Floodplain Channel Connectivity on Flood Hydrodynamics

Scott R. David[1,2], Jonathan A. Czuba[3], Douglas A. Edmonds[2], and Adam S. Ward[4]

[1]Department of Geosciences, University of Massachusetts, Amherst, Massachusetts, USA

[2]Department of Earth and Atmospheric Sciences, Indiana University, Bloomington, Indiana, USA

[3]Department of Biological Systems Engineering and The Global Change Center, Virginia Tech, Blacksburg, Virginia, USA

[4]School of Public and Environmental Affairs, Indiana University, Bloomington, Indiana, USA

Contents of this file

Introduction

This supporting information file contains an extended description of the methods that are unique to this study and those that partially overlap with Czuba et al. (2019)

Text S1: 1.0 Extended Methods

1.1.0 Model Development

We developed a 2-D unsteady surface-water hydrodynamic model for the East Fork White River and its adjacent floodplain in HEC-RAS version 5.0.3 using the Saint Venant equations. The computational mesh contained a total of 187,955 cells and used a combination of structured and unstructured meshes. The structured computational mesh has square cells, each 900 m^2. Breaklines were enforced along major roadways (cell spacing of ~3m), river banks, middle of the river (cell spacing of ~12m), and across the low head dam (cell spacing of ~1.5m; Figure S1) producing the unstructured portion of the mesh. A spatially varied Manning's

roughness was applied to the mesh, based on 30 m resolution land cover data (Homer et al., 2015),and the coefficients were chosen based on model calibration discussed in section 1.2. The topography data used in the model was a 1.5m digital elevation model (DEM) derived from light detection and ranging (lidar) data, bathymetric data, and theoretical topography for connectivity scenarios constructed by modifying the empirical elevation datasets. The topographic and bathymetric data collection and manipulation is described in section 1.1.1. Boundary conditions were set at three locations on the model grid: the upstream model extent of the East Fork White River, the upstream model extent of Sand Creek, and the downstream model extent of the East Fork White River (Figure S1). Our choice in boundary conditions is discussed in section 1.1.2.

1.1.1 Topography and Bathymetry Data

Topographic data used in the model consisted of a combination of empirical and theoretical topographic datasets. The empirical data used were constructed from a 1.5m DEM derived from aerial lidar flown on March 23, 2011 (http://www.indianamap.org). The lidar sensor could not measure topography through surface water, hence data points with water on the day of data acquisition were removed and replaced with a flat or sloping plane, a process called hydro-flattening. But the geometry of the main channel is important for the flooding processes we seek to understand here. We surveyed the river channel using a single-beam acoustic profiler measuring water depth and spatial location. The portion of the reach we surveyed is shown with a yellow line in figure 1. Additionally, we measured water-surface profiles with a real-time kinematic geographic position system (RTK-GPS) along the river during the day of surveying. To construct the bed-elevation surface we subtracted the depth data from the measured water-surface elevation data. Bed elevation data were processed into a DEM by taking the average depth along 30 m (approximately half the average river width) segments of the river centerline. The average depth along the segment was then assigned to a cross-section along that river segment. A triangulated irregular network was generated from the cross-sections, averaging all cross-channel variability while maintaining down-valley pool and riffle sequences. River reaches without bathymetric data were lowered by 1.5m to match the overall slope of our measured bathymetric data.

In addition to the actual topography, we also generated five synthetic floodplains based on the East Fork White River floodplain with various degrees of floodplain channel and river-floodplain connectivity. The synthetic floodplain surfaces were generated by extracting the extent of the East Fork White River active floodplain at the 89-year flood of record. We then removed all floodplain channels from the floodplains surface by applying a Gaussian filter (Eqn. 1) as:

$$G(x,y) = \frac{1}{\sqrt{2\pi\sigma^2}} e^{-\frac{x^2+y^2}{2\sigma^2}} \quad \text{Eqn. 1}$$

where, x and y are spatial distances (meters) and σ is the standard deviation of the Gaussian distribution. The calculation used σ = 6 m and iterated over the active floodplain 20 times, creating a preliminary smoothed floodplain. The presence of the floodplain channels caused artificially low inter-channel areas during the spatial averaging. To overcome this, we removed and interpolated all portions of the active floodplain ~0.1m lower than the preliminary smoothed surface. This eliminated most floodplain channels and the river channel. Additionally, we removed all major road features in the active floodplain domain to avoid any artificial increases

in floodplain elevation. We applied the same Gaussian filter as before to the active floodplain with the floodplain channels, river channel, and roads removed, thus producing a smoothed version of the East Fork White River floodplain that maintains long wavelength topography. The river channel, roads, and terraces were then added back into the smoothed floodplain topography creating a floodplain with a similar long wavelength topography and floodplain extent, but without floodplain channels (Figure 2).

We used the smoothed floodplain (Figure 3a) and existing floodplain (Figure 3f) to generate four additional floodplains with different topographic connectivity between the floodplain channels and the river channel. We envision different floodplain-channel network connectivity as being related to the degree of channelization. The present floodplain surface is channelized with a highly integrated floodplain-channel network, and the smooth floodplain surface is the least channelized. We create intermediately channelized floodplains by selectively preserving the deepest parts of the channel network. This creates a floodplain with channel segments that are not connected. To do this we detrend the natural floodplain with the smoothed floodplain, thereby creating a normalized DEM where negative values represent elevations lower than the smoothed floodplain. We then use two floodplain channel masks with threshold values of -0.23 m and -0.84 m and remove all channel cells above the thresholds. This creates two surfaces that isolate and preserve only the lowest-lying floodplain channel cells (threshold of -0.84 m) and both low-lying and mid-elevation floodplain channels (threshold of -0.23 m). The two channel masks were used to extract floodplain channels from the existing topography and add them back to the smoothed floodplain topography. The threshold of -0.84 m created a floodplain with weakly connected floodplain channels (Figure 4c), and the threshold of -0.23 m created a floodplain with better connected floodplain channels (Figure 4e).

Additionally, we constructed two synthetic floodplains with the same floodplain-channel connectivity as described above, but we also changed the strength of connections between the floodplain channel and the main river (Figure 3b, d). To accomplish this, all floodplain channels were removed from the two floodplain channel masks within 60 m (approximately two times the average levee width) of the river channel. This effectively removes all natural breaks in the levees and banks created by channels or crevasses. We created one additional floodplain channel mask to delineate the floodplain channels on the existing floodplain using a threshold of -0.15 m. The mask was used for data analysis and quantifying initial conditions.

To quantitatively describe our six different initial conditions, we developed a metric to describe the connectivity within the floodplain-channel networks (hereafter down-valley connectivity, DVC). DVC was calculated as:

$$DVC = \frac{F_{CA}}{F_{TA}} \times F_I \qquad \text{Eqn. 2}$$

where, F_{CA} is the floodplain channel surface area (m^2), F_{TA} is the total floodplain area (m^2), and F_I is the number of floodplain segments surrounded by floodplain channels (an approximation to assess the number of floodplain channel connections). F_{CA} was calculated with the floodplain channel masks used to extract floodplain channels (described above). F_{TA} was measured based on the wetted extent of the 89-year flood (peak of record) from Czuba et al., (2019). Hence, larger DVC values indicate a greater number of well-connected floodplain channels across the floodplain.

Similarly, we describe the connectivity between the floodplain and main channel as river-floodplain connectivity (RFC). RFC was computed as the coefficient of variation (standard deviation/mean) of the bank height within 30 m (approximately average levee width) of the river channel (Figure 3g). Larger RFC values represent river banks with higher topographic variability, hence an enhanced connection of the river channel to floodplain channels.

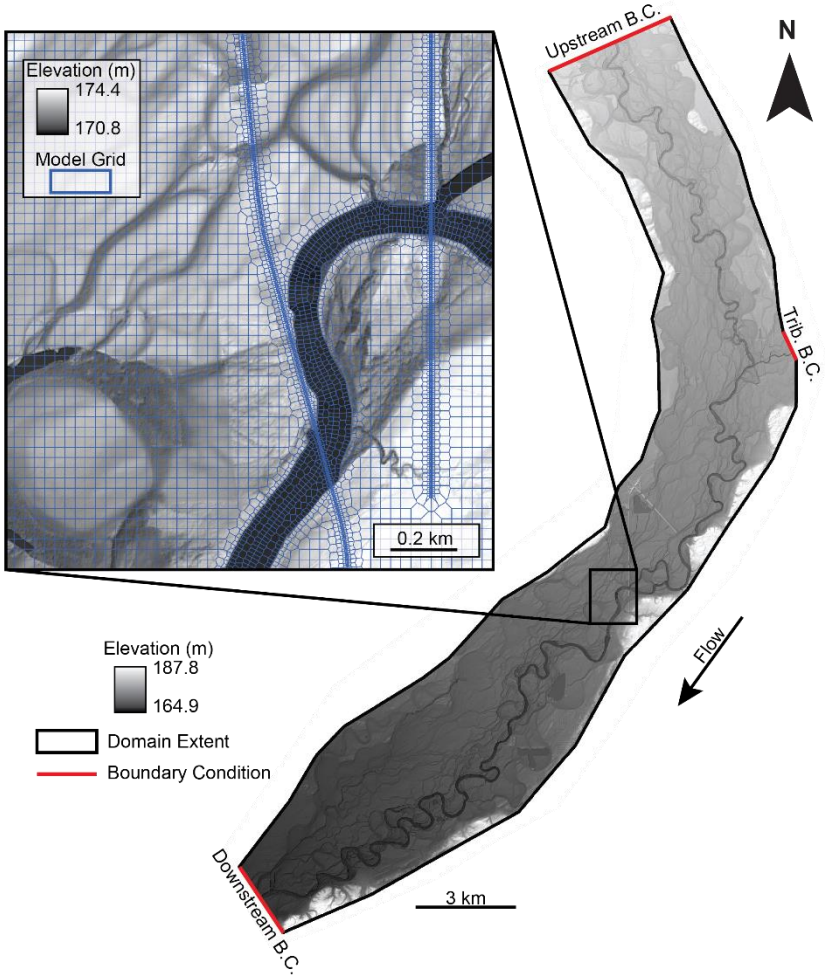

Figure S1*. Model setup along the East Fork White River. The inset shows an example of the computational grid used in the study. Note the floodplain contains a structured grid, while the river and roads have unstructured grids. Locations of the boundary conditions are shown with red lines.*

1.2 Boundary Conditions

The upstream boundary conditions were specified along the East Fork White River and Sand Creek (Figure S1) as a quasi-steady state discharge entering the domain. The quasi-steady state simulations held the discharge entering the domain constant until equilibrium was achieved throughout the entire domain before increasing the discharge (Figure 3h). Discharge entering the domain at the upstream boundaries was chosen based on modeling work by Czuba

et al. (2019), which simulated a variety of discharges (7-day to 89-yr. recurrence interval; RI) on the same reach of the East Fork White River. For our modeling experiments, we used six different discharges ranging from 292 m^3s^{-1} to 2,730 m^3s^{-1} which spanned a range of floodplain inundation extents (Figure 3h). Discharges were specified as 90% of the flow entering the domain from the East Fork White River and 10% entering along Sand Creek, based on comparing relative drainage areas. The downstream boundary was specified along the downstream extent of the East Fork White River and its floodplain was set as normal depth (Figure S1). The computation of normal depth required a friction slope (energy grade line slope) which was set to 0.001 along the boundary. The six simulated discharges and six initial conditions created a total of 36 simulations exploring steady state discharges. Additionally, we ran six simulations for unsteady discharges using the smoothed and existing topography. For the unsteady simulations, we specified no discharge entering the domain along the Sand Creek boundary condition and specified a hydrograph at the upstream boundary for the East Fork White River. The input hydrographs were triangular shaped that had peak discharges of 292 m^3s^{-1}, 581 m^3s^{-1}, and 1467 m^3s^{-1}, respectively. The rising limb of the floodwave increased at a rate of 18.7 m^3s^{-1} per hour and the falling limb decreased at a rate of 8.2 m^3s^{-1} per hour. The rates for rising and falling floodwave limb is based on a 10-year average of all rising and falling limbs of floodwaves at the gage in Seymour, IN (USGS, 2018; Figure 9).

1.3 Calibration and Validation

We calibrated the model to the elevation-discharge rating curve developed for the USGS gage located near Seymour, IN (USGS, 2018; Figure 1). Model calibration was conducted by varying Manning's roughness coefficients for the open water (river channel) and agricultural land cover classes (Homer et al., 2015). Final roughness coefficients for the open water and agricultural land cover classes were 0.022 and 0.025 (Table S1), respectively. The final calibrated roughness coefficients in our study differs from those in Czuba et al. (2019) due to the use of the Saint Venant equations rather than the diffusive wave equations. Comparing our model simulations to the elevation-discharge rating curve, we obtained a root mean squared error (RMSE) of 0.16 m and a mean average error (MAE) of 0.15 m. The error we obtained from our model simulations was within the error of the USGS field data used to compute the elevation-discharge rating curve (RMSE= 0.26 m, MAE = 0.18 m; Figure S2a).

Land cover class	Default *n*	Final *n*
Agricultural Vegetation	0.04	0.025
Open Water	0.035	0.022
Forest & Woodland	0.12	0.12
Undifferentiated Barren Land	0.04	0.04
Developed, Open Space	0.04	0.04
Developed, Low Intensity	0.08	0.08
Developed, Medium Intensity	0.1	0.1
Developed, High Intensity	0.15	0.15

Table S1. Land cover classes and their associated Manning's Roughness coefficients (*n*). The table shows the default Manning's Roughness coefficients (Brunner, 2016) based on land cover classes and our final coefficients after calibration.

Model validation was accomplished using surveyed high-water marks collected by the USGS in 2008 (Morlock et al., 2008), water-surface elevations collected during flooding in February, 2018, and aerial imagery of flooding collected in April, 2011 (locations shown in Figure 1). The 2008 high-water marks were measured using mud, drift, debris, and seed lines on trees, fences, buildings, and utility poles (Morlock et al., 2008) as a proxy for maximum water-surface elevation. The measurements corresponded to the peak of record on June 8, 2018 with a discharge of 2,730 m^3s^{-1}. The 2018 water-surface elevations were measured on February 26, 2018 using RTK-GPS and corresponded to a flow of ~890 m^3s^{-1} at the USGS gage in Seymour, IN. Comparing our model simulation of the existing topography to the measured high-water marks gave a RMSE of 0.51m and a MAE of 0.46m (Figure S3b). A comparison between our model simulation and direct measurements of water-surface elevations collected in 2018 was more accurate with a RMSE of 0.17 m and a MAE of 0.12 m (Figure S3b).

The aerial photo of flooding (Figure S2c) was taken on April 7, 2011 at ~12:30 pm corresponded to a discharge of ~657 m^3s^{-1} and a water-surface elevation of 127.7 m at the USGS gage in Seymour, IN. Comparing our model simulation with a discharge of ~657 m^3s^{-1} and a water-surface elevation of 172.9 m (at the location of the river gage) to the aerial imagery, the simulation slightly over-predicts the extent of inundation, but still captures the majority of land-water transitions (Figure S2d) in high detail.

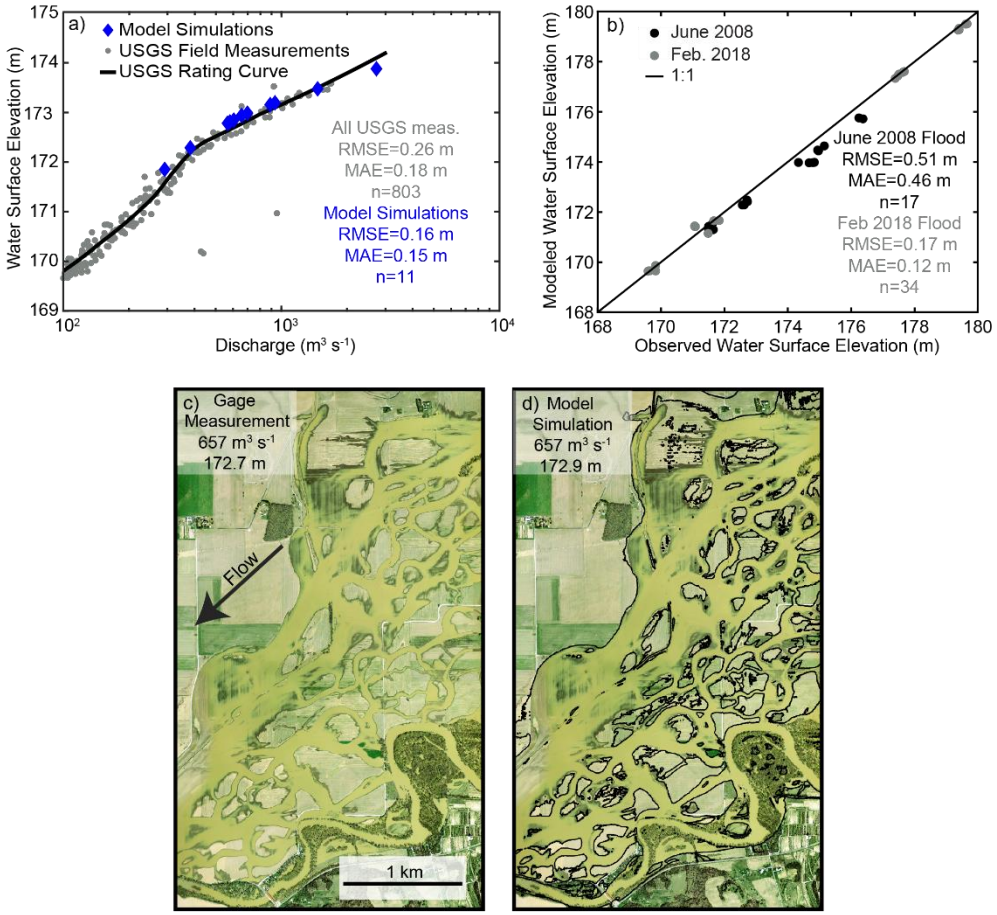

Figure S2. *Model calibration and validation data. a) Model calibration to the elevation-discharge rating curve, gage location is shown in Figure 1. b) Simulated vs. measured water surface elevations for high water marks measured from the peak record flood in June 2008 and water surface elevations from flooding on Feb. 26, 2018. c) Aerial photography of flooding on April 7, 2011. d) Model simulation showing transition of water to land as black lines corresponding to the same discharge when the image was taken.*

3.3 Data Analysis

Initial model outputs from our 36 modeling experiments included water depth, depth averaged velocity magnitude, and 2-D (x and y directed) depth averaged velocity for each cell. We gridded the results at a 15-m resolution for all analysis. From the initial model outputs, we computed the magnitude of specific discharge (q, Eqn. 3) and a 2-D specific discharge ($q_{x,y}$; Eqn. 4) for each grid cell in all model simulations as:

$$q = \bar{v} * h \qquad \text{Eqn. 3}$$

and

$$q_{x,y} = \overline{v_{x,y}} * h \qquad \text{Eqn. 4}$$

where, $\bar{v}$ is the depth-averaged magnitude of velocity (m s^{-1}), h is water depth (m), and $\overline{v_{x,y}}$ is the 2-D depth-averaged velocity in the x or y direction, respectively (m s^{-1}).

To assess the flooding extent in each of our modeling simulations, we produced water masks from our depth data. Water masks were constructed by converting the gridded depth data into polygons and merging the depth polygons into a single polygon representing the wetted extent of the floodplain. The wetted extent polygons were then used to compute the percent of the floodplain that was inundated. Additionally, water masks were used to compute the number and area of hydrologic islands in the domain. Hydrologic islands are defined as dry areas surrounded by water.

We measured the average flooding depth, velocity magnitude, and specific discharge magnitude in the river channel, entire floodplain, and floodplain channels. This was accomplished using a polygon mask of the river channel, entire floodplain extent, and floodplain channel masks used to generate the initial conditions (section 3.2.1). Averages and standard deviations were computed as the mean and standard deviations for a half-Gaussian distribution for all cells within the extent of a polygon. Trend significance of the results were evaluated using a F-test.

We computed an average lateral exchange of surface water between the river channel and floodplain for each steady state model run. Lateral exchange was measured perpendicular to lines situated parallel and positioned 30 m (approximate levee width) from the river banks. The lines were discretized into 90 m long segments and the average q_x and q_y were calculated over each 90m line segment. Between vertices, along the 90 m line segment, we used vector decomposition to solve for the magnitude of specific discharge perpendicular to each line segment (q_p, m s^{-1}), where positive q_p values indicate a flux into the river channel and negative values indicate a flux into the floodplain. The average lateral exchange for each side of this river ($\overline{q_{ex}^{L,R}}$, *L* is river left and *R* is river right) is calculated as:

$$\overline{q_{ex}^{L,R}} = \left(\sum_j \left|q_j^{L,R}\right| d_j^{L,R}\right) \frac{1}{D^{L,R}} \quad \text{Eqn. 5}$$

where, $d_j^{L,R}$ (meters) is the length of individual line segment *j* and $D^{L,R}$ (meters) is the total distance of all line segments along a given side of the river. The absolute value was taken to account for all flux between the river channel and floodplain. Whereas if the absolute value was not taken, we would compute a net flux between the river and floodplain giving a value of ~0, as flow entering the river and exiting the river would negate each other. The lateral exchange through the left and right side of the river were added together and normalized by the average specific discharge in the river channel ($\overline{q_r}$) to produce normalized unitless river-floodplain exchange (q_{ex}; Eqn. 6).

$$q_{ex} = \frac{\overline{q_{ex}^{L}} + \overline{q_{ex}^{R}}}{\overline{q_r}} \quad \text{Eqn. 6}$$

To assess the unit residence time of water in the floodplain, we used a defined network of simulated flow paths that were manually traced by Czuba et al. (2019) in the upper portion of our domain. Flow paths were delineated by systematically increasing discharge, and all new flow paths were traced for each increase in flow. In total, there were 23,211 paths mapped with a cumulative distance of ~1,050 km (Figure S3). Average flow velocity (v_i; m s^{-1}) was calculated

for each line segment that existed in the wetted extent of each model simulation. A length-averaged velocity ($\overline{v_f}$; m s^{-1}) in the floodplain over all the line segments was computed as:

$$\overline{v_f} = \frac{(\sum v_i l_i)}{L} \quad \text{Eqn. 7}$$

where, l_i is the length of a line segment and L is the length of the total active flow paths. A residence time per unit length of floodplain (t_f; s m^{-1}) was calculated as the inverse of v_f, which describes the time water spends along a certain length scale. Additionally, we calculated a residence time per unit length for the river (t_c; s m^{-1}) by taking the inverse of the average magnitude of velocity in the river channel. We normalized unit residence time (t_r) by the residence time in the river, creating a unitless residence time in the system as:

$$t_r = \frac{t_f}{t_c} \quad \text{Eqn. 8}$$

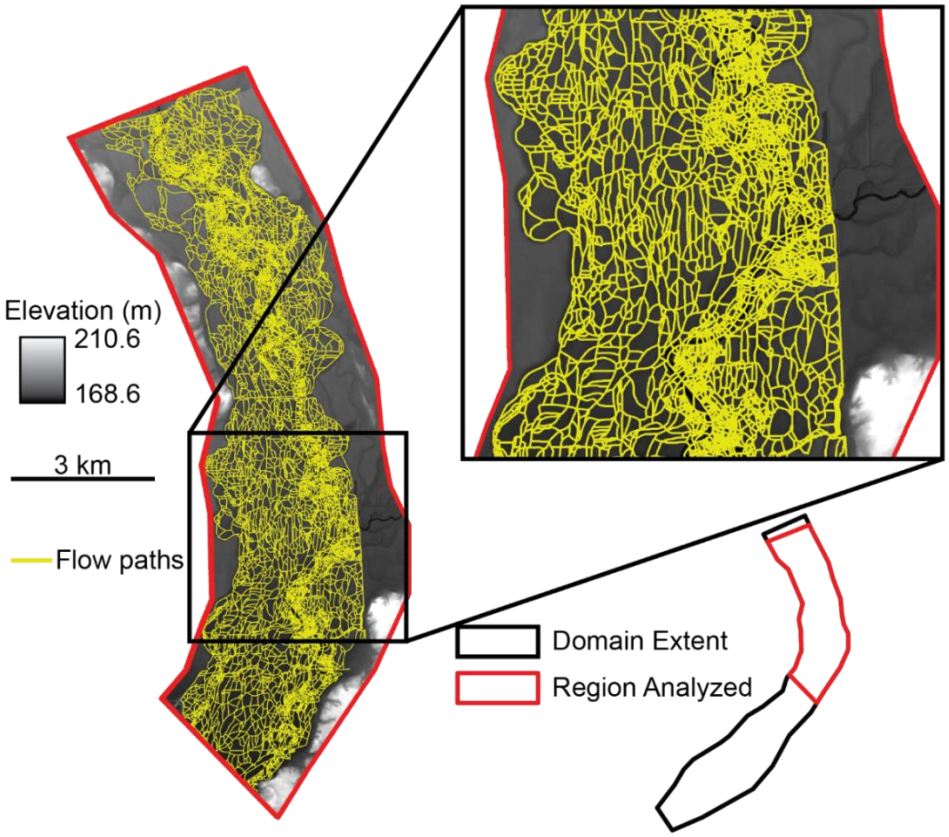

Figure S3. *Flow paths for unit residence time calculation. The yellow lines show the flow paths delineated by Czuba et al. (2019), used to compute the average unit residence time in the floodplain. The portion of the domain for which the analysis was performed is shown in red and the entire model domain is shown in black.*